Behavior of the nuclear charge radii systematics in the *s-d* shell from muonic atom measurements

G. Fricke, J. Herberz, Th. Hennemann, and G. Mallot
Institut für Kernphysik der Universität Mainz, D-6500 Mainz, Germany

L. A. Schaller, L. Schellenberg, C. Piller, and R. Jacot-Guillarmod
Institut de Physique de l'Université, CH-1700 Fribourg, Switzerland
(Received 4 September 1991)

The present work extends the systematics of nuclear charge radii obtained by the method of muonic atoms to nuclei with $8 \leq Z, N \leq 20$. The accuracy of the measured muonic Lyman transition energies of generally ≤ 10 eV leads to a precision in the model-independent nuclear charge radii differences of 2–3 am for the isotope shifts and 4–9 am for isotone shifts. Both isotope and isotone shifts within the *s-d* shell behave "anomalously" with respect to the systematics of heavier nuclei. However, such behavior is predicted on theoretical grounds, if mixing in the *s-d* shells and the strong deformation of some of the nuclei in this region are considered. We compare charge radii from elastic electron scattering data with muonic atom rms radii and suggest that observed deviations are possibly due to incomplete dispersion corrections.

PACS number(s): 21.10.Ft, 36.10.Dr, 27.20.+n, 27.30.+t

I. INTRODUCTION

In recent years, our collaboration including the group of E. B. Shera at Los Alamos National Laboratory has performed precision measurements of nuclear charge radii using the muonic atom method. Both absolute nuclear charge radii and charge radii differences have been measured. A detailed comparison of isotope shifts and isotone shifts with different theoretical models has been made. In heavier nuclei, mean-field theories are often employed [1–4], and an extensive systematics with several typical features can be established [5–12]. In lighter nuclei, however, mean-field theories are not adequate. Nuclei in the *s-d* shell, i.e., with nucleon numbers $8 \leq Z, N \leq 20$, show considerable ground-state correlations between protons and neutrons. Hence, they are not built upon a hard core ^{16}O nucleus. In addition, due to large deformation parameters, e.g, $\beta = 0.5$ for neon and sodium, and a deformation jump from a strong prolate to a strong oblate shape at ^{28}Si, no normal systematic behavior can be expected.

The present work deals with a systematic comparison of nuclear ground-state charge radii and their differences in the region of the $1d_{5/2}$, $2s_{1/2}$, and $1d_{3/2}$ shells using the muonic atom method. In particular, we have studied the isotopes ^{16}O, ^{19}F, ^{20,21,22}Ne, ^{23}Na, ^{24,25,26}Mg, ^{27}Al, and ^{nat}Si. The present analysis also includes results from our earlier measurements on ^{12,13,14}C [13,14], ^{31}P, ^{32,34,36}S [15], ^{36,38,40}Ar [16], and ^{39,41}K, ^{40,42}Ca [12]. The isotope shift between ^{18}O and ^{16}O is taken from the work of Backenstoss *et al.* [17]. The results from Ehrlich [18] on ^{28,29,30}Si are used in the analysis of our ^{nat}Si measurements. The elastic electron scattering results of de Vries *et al.* on ^{15}N (Ref. [19]), Miska *et al.* on ^{16,17}O (Ref. [20]) and Briscoe *et al.* on ^{35,37}Cl (Ref. [21]) have also been used.

Section II describes the experimental setup and the determination of the transition energies in the various nuclei. Section III shows how the nuclear charge radii and the differences between isotopes or isotones are evaluated. Section IV compares our results with data from elastic electron scattering. Section V presents our isotope and isotone shift results within the *s-d* shell and compares them with the systematics obtained for heavier nuclei. Finally, Sec. VI interprets the nuclear charge radii differences for nuclei with $8 \leq Z, N \leq 20$ in terms of mixed shell structure and deformation.

II. EXPERIMENT AND ANALYSIS

The muonic atom measurements have been performed at the superconducting μE1 channel of the Paul Scherrer Institute (PSI) at Villigen, Switzerland. The experimental setup has been described elsewhere [9,22,23]. Here we only mention details which are peculiar to the present experiment.

To reduce systematic experimental errors, the calibration was performed on line, and several targets were measured simultaneously, in various combinations. Two different target arrangements were used depending on the physical states of the elements. For the measurements on gaseous elements (neon and argon), a high-pressure hydrogen gas target (200 bars), which takes advantage of the muon transfer from hydrogen to the noble gas, was used [24]. The negative muons are stopped in hydrogen and are subsequently transferred to the noble gas atoms X, by means of the process $(\mu^- p) + X \rightarrow p + (\mu^- X)^*$. This method allows us to study rare isotopes like ^{21}Ne, ^{36}Ar, or ^{38}Ar. A simultaneous collection of muonic x-ray calibration lines, e.g., from oxygen and aluminum, could be achieved by placing solid targets inside the high-pressure gas target. Their energy spectra were separated from the noble gas spectra by using the fact that muonic x rays from solids appear promptly (within about 20 ns)

after a muon stops in the target, while the transfer process produces a delay. When all solid isotopes were measured, a parallel arrangement of three single targets was employed, which takes advantage of the 6×4 cm^2 cross-sectional area of the muon beam [9]. Target combinations have been chosen redundantly. The separation of the x rays from each of the three targets was achieved by the prompt timing signals from the individual scintillation counters which were placed in front of each target.

The muonic x rays were measured with a 10 cm^3 Ge diode that had a resolution of 1.1 keV at an energy of 300 keV. On-line energy calibrations were made using radioactive sources with well-known γ-ray energies, namely ^{75}Se, ^{133}Ba, and ^{182}Ta [25,26]. The calibration lines appeared as accidental coincidences in the delayed spectra. Cross checks using the magnesium and aluminum muonic Lyman series transitions were also performed. The electronic setup is described in more detail in [22,23]. Both energy and time information relative to the stopped muon were digitalized and processed by the program DAVID [27] via CAMAC and a PDP-11/40 computer. The latter also provided on-line experiment control.

The centers of gravity of the γ lines of interest were determined using the computer codes DISPLAY and MYFIT [28]. As an example, Fig. 1 presents a fit of the muonic ^{nat}Mg $2p\rightarrow1s$ transitions. To determine the center of this complex, the calculated fine-structure splittings ($\Delta p=2p_{3/2}-2p_{1/2}=195$ eV) and the calculated relative intensities were used for the three isotopes ^{24,25,26}Mg present in ^{nat}Mg. Fitting the measured spectra of the enriched isotopes ^{25}Mg and ^{26}Mg (enrichment $>99\%$) resulted in a χ^2/F value of approximately 1.

Figure 2 shows a prompt-plus-delayed sum spectrum from the ^{22}Ne gas target (the ^{22}Ne muonic Lyman series and the ^{182}Ta and ^{75}Se calibration lines). The neon transitions appear delayed with respect to the stopped muon due to the transfer mechanism used in the high-pressure hydrogen target as discussed earlier. Only 1 1 of 99.96% enriched ^{22}Ne gas at STP was employed, which yielded a concentration ratio for Ne to H_2 of 8.5×10^{-4}. For ^{21}Ne, a five times smaller concentration still yielded precise data [22].

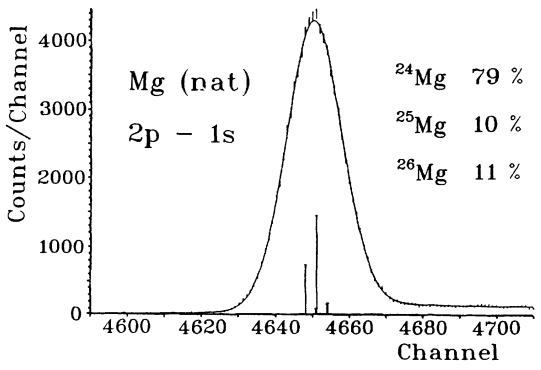

FIG. 1. Computer fit of the Mg $2p\rightarrow1s$ complex, measured in prompt coincidence with the incoming muons. Since for the measurement of ^{24}Mg a natural magnesium target was used, the corresponding transitions of ^{25}Mg and ^{26}Mg are also shown. The lengths of the bars correspond to the relative intensities. The detector resolution is about five times larger than the (calculated) fine-structure splitting of 195 eV.

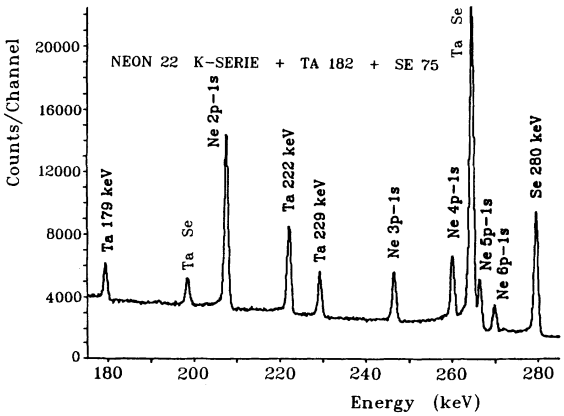

FIG. 2. Sum spectrum (prompt plus delayed) of the ^{22}Ne K series including ^{75}Se and ^{182}Ta calibration lines. The neon transitions appear mostly delayed with respect to a stopped muon, since the transfer mechanism $\mu^-p+\mathrm{Ne}\rightarrow(\mu^-\mathrm{Ne})^*+p$ was used.

Table I lists the experimental transition energies of the muonic Lyman series of all stable isotopes (with the exception of ^{17}O) from ^{16}O to ^{30}Si. The $np_{3/2}\rightarrow1s_{1/2}$ energies, which are determined from the measured np-$1s$ center-of-gravity energy values, using calculated fine-structure splittings and intensity ratios, are given. The final errors quoted for these values include statistical errors, uncertainties of the calibration energies, and nonlinearity corrections for the ADC. For the most intense $2p$-$1s$ transitions, the errors are less than 10 eV with the exception of the rare Si isotopes, where they are about five times larger, due to the employment of a natural silicon target in connection with older isotope shift measurements [18]. The other columns of Table I will be discussed in the next section.

III. EVALUATION OF NUCLEAR CHARGE RADII AND CHARGE RADII DIFFERENCES

In order to obtain nuclear ground-state charge radii, the measured transition energies have to be compared with calculated values. To the former energies, the nuclear recoil energy has to be added, according to

$$E(|i\rangle\rightarrow|f\rangle)=E_\gamma+E_\gamma/(2Mc^2)\ ,$$

where E_γ is the measured energy for the muonic transition $|i\rangle\rightarrow|f\rangle$ and M stands for the nuclear mass. For the isotopes considered in this work, this correction amounts to at most $+5$ eV.

The latter energies are evaluated by numerically solving the Dirac equation of the muon-nucleus system [29] using an explicit form for the nuclear charge density $\rho(r)$. In general, a two-parameter Fermi distribution

$$\rho(r)=1/\{1+\exp[(r-c)/a]\}$$

is used, where the diffuseness parameter a is related to the skin thickness t by $t=4(\ln3)a$ and c is the half-density radius.

Although the finite nuclear charge extension is the largest correction to the Dirac point nucleus energies in the 1*s* states of the muonic atoms considered here, several additional corrections have to be calculated. This is done by adding additional potentials to the Hamiltonian operator. The most important correction is the vacuum polarization, of the order of the fine-structure constant α smaller than the muonic 1*s* energy. In addition, there are vacuum polarization corrections of higher order, other QED corrections like Lamb shift or anomalous magnetic moment, and electron screening corrections. The relativistic treatment of muonic atoms as a two-body problem requires also, besides the introduction of a reduced mass, an additional recoil correction. Finally, there is a correction due to virtual nuclear excitations, analogous to the dispersion corrections in electron scattering. The dynamical interaction between muon and nucleus leads to a mixture of muonic and nuclear states, the so-called "nuclear polarization" effect. The contributions due to low-lying nuclear excited states are explicitly taken into account by the $B(E\lambda)$ matrix elements, while for the high-lying states, averaging over the isoscalar and isovector giant resonances with multipolarities $0 \leq \lambda \leq 3$ is performed. The nuclear polarization calculations have the largest uncertainty of all corrections, typically 20–30 % for absolute nuclear charge radii and 10% for isotope or isotone shifts [30,31]. The total nuclear polarization corrections amount to 5 eV for the 1*s* state of ^{16}O and to 55 eV for the 1*s* state of ^{30}Si. Table II shows as an example the Dirac point nucleus energy and all corrections in the case of the muonic 1*s* levels in ^{24}Mg, ^{26}Mg, and ^{28}Si.

According to a method first developed by Barrett [32], the differences ΔV_{if} of the muon potentials in the initial (i) and final (f) states are practically independent of the

TABLE I. Experimental $np_{3/2}$-$1s_{1/2}$ transition energies. The quoted error includes statistical errors, uncertainties of the calibration energies, and nonlinearity corrections. Fits for the half-density radius c were made using two-parameter Fermi charge distributions with a fixed $t = 2.30$ fm. The deduced rms radii are only slightly model dependent due to the low Z. The uncertainties for the nuclear polarization correction are included in the given error for the Barrett equivalent radius $R_{k,\alpha}$.

	Transition	Experimental energy $np_{3/2}$-$1s_{1/2}$ E_{exp} [eV]	Half-density radius c (fm)	rms radius (fm)	k α (fm^{-1})	$-C_z$ (am/eV)	Barrett radius $R_{k,\alpha}$ (fm)
^{16}O	$2p \rightarrow 1s$	133 544(4)	2.4174(46)	2.703	2.0285	1.285	3.476(8)
	$3p \rightarrow 2s$	158 425(4)			0.0261		
	$4p \rightarrow 1s$	167 128(5)					
^{18}O	$2p \rightarrow 1s$	133 572(9)	2.554(13)	2.778	2.0287	1.258	3.568(14)
	$3p \rightarrow 1s$	158 469(19)			0.0258		
	$4p \rightarrow 1s$	167 179(23)					
^{19}F	$2p \rightarrow 1s$	168 535(6)	2.7819(37)	2.902	2.0367	0.782	3.731(6)
	$3p \rightarrow 1s$	200 055(5)			0.0292		
	$4p \rightarrow 1s$	211 091(6)					
^{20}Ne	$2p \rightarrow 1s$	207 314(10)	2.9569(68)	3.005	2.0445	0.517	3.864(8)
					0.0329		
^{21}Ne	$2p \rightarrow 1s$	207 461(19)	2.8934(69)	2.968	2.0441	0.520	3.816(8)
					0.0330		
^{22}Ne	$2p \rightarrow 1s$	207 544(19)	2.8699(69)	2.954	2.0439	0.1522	3.798(8)
					0.0330		
^{23}Na	$2p \rightarrow 1s$	250 278(7)	2.9361(23)	2.993	2.0484	0.365	3.847(6)
	$3p \rightarrow 1s$	297 474(13)			0.0361		
	$4p \rightarrow 1s$	313 967(8)					
^{24}Mg	$2p \rightarrow 1s$	296 602(5)	3.0440(14)	3.057	2.0525	0.262	3.928(4)
	$3p \rightarrow 1s$	352 778(9)			0.0387		
	$4p \rightarrow 1s$	372 417(10)					
^{25}Mg	$2p \rightarrow 1s$	296 791(8)	2.9969(25)	3.029	2.0521	0.264	3.892(5)
	$3p \rightarrow 1s$	352 972(25)			0.0388		
	$4p \rightarrow 1s$	372 637(23)					
^{26}Mg	$2p \rightarrow 1s$	296 813(6)	3.0069(18)	3.035	2.0522	0.263	3.899(5)
	$3p \rightarrow 1s$	353 009(15)			0.0387		
	$4p \rightarrow 1s$	372 652(19)					
^{27}Al	$2p \rightarrow 1s$	346 926(7)	3.0534(13)	3.062	2.0571	0.196	3.934(4)
	$3p \rightarrow 1s$	412 903(10)			0.0418		
	$4p \rightarrow 1s$	435 992(12)					
^{28}Si	$2p \rightarrow 1s$	400 295(9)	3.1529(14)	3.122	2.0620	0.149	4.010(4)
	$3p \rightarrow 1s$	476 860(12)			0.0446		
^{29}Si	$2p \rightarrow 1s$	400 375(45)	3.1482(86)	3.120	2.0620	0.149	4.006(9)
^{30}Si	$2p \rightarrow 1s$	400 295(44)	3.1720(84)	3.134	2.0622	0.149	4.025(9)
					0.0446		

TABLE II. $1s_{1/2}$ binding energies and corrections for muonic ^{24}Mg, ^{26}Mg, and ^{28}Si (in eV).

	^{24}Mg	^{26}Mg	^{28}Si
Point nucleus energy	403 977.6	404 123.9	550 611.6
Vacuum polarization			
order $\alpha(Z\alpha)$	2 216.0	2 218.9	3 179.2
order $\alpha^2(Z\alpha)$	16.8	16.8	24.3
order of $\alpha(Z\alpha)^n$, $n \geq 3$	−0.9	−0.9	−1.6
μ-vacuum polarization	4.3	4.3	7.3
Relativistic recoil	6.4	5.9	10.5
Electron screening	0.0	0.0	0.0
Nuclear polarization	37.0	37.0	55.0
Finite-size effect	−8 544.5	−8 445.5	−15 791.0
Binding energy $1s_{1/2}$	397 662.2	397 909.7	538 012.4

form of the chosen charge density $\rho(r)$. Each muonic transition can thus be associated with a different, but model-independent radial moment k,α of the nuclear charge distribution, the so-called Barrett moment:

$$\langle r^k e^{-\alpha r}\rangle = 4\pi \int_0^\infty \rho(r) r^k \exp(-\alpha r) r^2 dr \ .$$

The parameter α is kept fixed for each element. The radius of a homogeneously charged sphere $R_{k,\alpha}$ yielding the same Barrett moment is then given by

$$3(R_{k,\alpha})^{-3} \int_0^{R_{k,\alpha}} r^k e^{-\alpha r} r^2 dr = \langle r^k e^{-\alpha r}\rangle \ .$$

Table I presents, for the s-d shell elements from ^{16}O to ^{30}Si, the rms radii $\langle r^2\rangle^{1/2}$ ($k=2,\alpha=0$) and the corresponding Barrett equivalent radii $R_{k,\alpha}$ as well as the fitted values of k and α [23]. The quoted errors for the Barrett radii contain not only statistical and nonlinearity errors, but also nuclear polarization uncertainties. Also shown are the sensitivities C_Z (in am/eV) of the Barrett radii to the measured $2p_{3/2}$-$1s_{1/2}$ transition energies. If the absolute energy errors are multiplied by C_Z, the corresponding errors in the radii are obtained. No errors are given for the rms radii, since these values cannot be determined model independently. However, for the rather light elements considered in this work, the differences of rms radii to equivalent Barrett radii are only of the order of $\frac{1}{2}$%, since the moment k is close to 2 and $\alpha \approx 0$.

Table III lists the rms and $R_{k,\alpha}$ radii differences (isotope and isotone shifts) for the same elements as in Table I. The given errors for the differences $\Delta R_{k,\alpha}$ contain also, analogously to the Barrett radii of Table I, nuclear polarization uncertainties, besides the statistical and nonlinearity errors. For a more complete discussion of error contributions see Ref. [23].

IV. COMPARISON WITH RESULTS FROM ELASTIC ELECTRON SCATTERING

Nuclear charge radii can also be determined by elastic electron scattering. A recent compilation of rms radii

TABLE III. Barrett equivalent radii and rms radii differences between neighboring nuclei ($\Delta N=2$, $\Delta N=1$ isotopes and $\Delta Z=2$, $\Delta Z=1$ isotones). For $\Delta R_{k,\alpha}$ all errors are included. The radii differences $\Delta R_{k,\alpha}$ for isotopes and isotones heavier than Si are displayed in Figs. 3 and 4 and contained implicitly in the odd-even staggering parameter γ (see Table V). No error is specified (see original publications [12–16,18]).

	Nuclei		$\Delta_{\rm rms}$ (am)	$\Delta R_{k,\alpha}$ (am)
$\Delta N=1$	^{20}Ne	^{21}Ne	−37	−48 (7)
	^{21}Ne	^{22}Ne	−14	−18 (7)
	^{24}Mg	^{25}Mg	−28	−36 (2)
	^{25}Mg	^{26}Mg	6	7 (3)
	^{28}Si	^{29}Si	−2	−4 (6)
	^{29}Si	^{30}Si	14	19 (6)
$\Delta N=2$	^{16}O	^{18}O	75	92 (10)
	^{20}Ne	^{22}Ne	−51	−66 (7)
	^{24}Mg	^{26}Mg	−22	−29 (2)
	^{28}Si	^{30}Si	12	15 (6)
$\Delta Z=1$	^{18}O	^{19}F	124	163 (14)
	^{19}F	^{20}Ne	103	133 (9)
	^{22}Ne	^{23}Na	39	49 (8)
	^{23}Na	^{24}Mg	64	81 (5)
	^{26}Mg	^{27}Al	27	35 (5)
	^{27}Al	^{28}Si	60	76 (4)
$\Delta Z=2$	^{18}O	^{20}Ne	227	296 (19)
	^{22}Ne	^{24}Mg	103	130 (9)
	^{26}Mg	^{28}Si	87	111 (6)

from elastic electron scattering can be found in [19]. In addition, we added the data of Knight *et al.* [33] on ^{22}Ne and the result of Soundranayagam [34] on ^{26}Mg. In general, the uncertainties of the rms radii extracted from elastic electron scattering are larger than those obtained in muonic atom work. Also, different electron scattering data for the same nucleus deviate often more than the quoted errors. Both facts are probably related to absolute normalization problems for electron scattering data. On the other hand, one should calculate our rms radii with the skin thickness t obtained from an (e,e) analysis. Utilizing such a procedure, when data are available, our rms radii of Table I—which are calculated with a fixed value of $t=2.30$ fm—shift, however, less than 2 am. This is due to the fact that for the relatively light nuclei of the s-d shell, rms and equivalent Barrett radii are very similar. Table IV compares our muonic atom radii r_μ with radii $r_{e,e}$ from elastic electron scattering data. One observes deviations in both directions of more than the given errors. More than one-third of the radii differences show such inconsistencies.

Before drawing conclusions about systematic deviations between these two methods [35], one should keep in mind that for elastic electron scattering data dispersion corrections have to be applied. In order to understand this situation, a detailed analysis including dispersion corrections calculated by Friar *et al.* [36] and elastic electron scattering measurements of the energy dependence of dispersion corrections for ^{12}C has been made by Offermann *et al.* [37]. In this analysis also the precise muonic x-ray data from ^{12}C measured with a crystal spec-

trometer [38] have been included. They came to the conclusion that the agreement of the results from these two methods is excellent in the case of ^{12}C.

V. BEHAVIOR OF NUCLEAR CHARGE RADII IN THE *s-d* SHELL

Due to the lesser accuracy of elastic electron scattering results and the lack of data from optical work, we shall concentrate in the following on a systematics of nuclear charge radii differences in the *s-d* shell obtained mostly from muonic atoms. Together with the results of Table III, we employ our former measurements on the isotopes of carbon, phosphorus, sulphur, and argon [13–16] and the radii data of other authors on oxygen, silicium, chlorine, potassium, and calcium [17,18,21,12]. In this way, a complete and accurate study of nuclear charge radii differences for practically all stable isotopes and isotones in the *s-d* shell becomes possible for the first time.

We first discuss the nuclear charge radii systematics when adding pairs of neutrons (isotope shifts), then when adding pairs of protons (isotone shifts). Finally, we study the so-called "odd-even staggering" effect.

TABLE IV. Comparison of elastic electron scattering radii $r_{e,e}$ with our muonic atom results r_μ. The differences of the radii $r_\mu - r_{e,e}$ are in 40% of the cases not in agreement within the given errors (see text).

Nucleus	rms radius μ atom (fm)	rms radius (e,e) (fm)	$r_\mu - r_{e,e}$ (am)
^{16}O	2.703(6)	2.728(8)	−25
		2.730(25)	−27
		2.718(21)	−15
^{18}O	2.778(11)	2.727(20)	+51
^{19}F	2.902(5)	2.900(15)	+2
^{20}Ne	3.005(6)	3.040(25)	−35
		3.004(25)	+1
		2.992(25)	+13
^{22}Ne	2.954(6)	2.951(27)	+3
		2.969(21)	−15
^{23}Na	2.993(5)	2.940(60)	+53
^{24}Mg	3.057(3)	3.080(50)	−23
		3.057(15)	0
		2.985(30)	+72
^{25}Mg	3.029(4)	3.110(50)	−81
		3.003(11)	+26
^{26}Mg	3.035(4)	3.060(50)	−25
		2.960(4)	+75
^{27}Al	3.062(3)	3.060(90)	+2
		3.050(50)	+12
		3.035(15)	+27
^{28}Si	3.122(3)	3.150(40)	−28
		3.086(18)	+36
		3.106(30)	+16
^{29}Si	3.120(7)	3.130(50)	−10
		3.079(21)	+41
^{30}Si	3.134(7)	3.176(22)	−42

A. Isotope shifts

The behavior of nuclear charge radii has been studied by our group together with Shera and his collaborators for nuclei above the *s-d* shell over the past years [5–12,24]. Several systematic regularities have become apparent if one looks at the differences of the Barrett equivalent radii $\Delta R_{k,\alpha}$ between two isotopes with N and $N+2$ neutrons at the respective abscissa values $N+1$ in the region $20 \leq N \leq 86$.

(1) For the same neutron number, the change of nuclear charge radii when adding a pair of neutrons is only weakly dependent on the respective proton configuration. This fact is not obvious, since nuclear radii are defined via radial moments of their ground-state charge distributions. Additional neutrons must therefore interact more strongly with the proton core than with the valence protons [5].

(2) After the closing of a magic neutron shell ($N=20$, 28, 50, or 82), there is a sudden increase of the radii differences, reflecting the shell structure of the atomic nuclei. In high-precision data, also subshell structures may be seen [8,9].

(3) In-between magic numbers, addition of a pair of neutrons results in an almost linear decrease of the radii differences $\Delta R_{k,\alpha}$. Even a shrinking of charge radii may be observed, e.g., just below the magic neutron number $N=50$ [5,6]. Such a decrease in $\Delta R_{k,\alpha}$ is generally related to a decrease in intrinsic nuclear deformation.

If we now apply the above-mentioned regularities to nuclei of the *s-d* shell, we obtain the dashed line of Fig. 3. Obviously, the real behavior of these nuclei is drastically different. The anomaly immediately starts at $N=8$ with

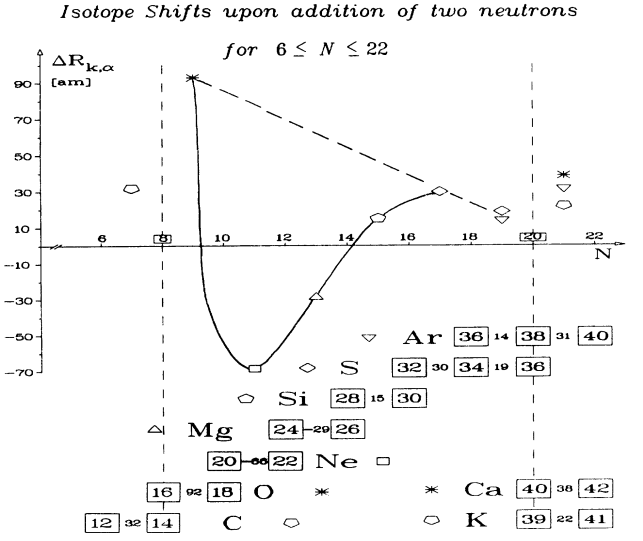

FIG. 3. "Anomalous" isotope shifts (see text) within the *s-d* neutron shell for even-even isotopes including the radii differences ^{14}C-^{12}C and ^{40}Ar-^{38}Ar. Plotted are the differences of the "model-independent" (see text) equivalent Barrett radii $\Delta R_{k,\alpha}$ between two neighboring isotopes with N and $N+2$ neutrons at the respective neutron numbers $N+1$. The drawn-in solid curve guides the eye. The dashed curve indicates the expected "normal" trend.

the radii difference between ^{18}O and ^{16}O, which is, with a value of +92 am, larger than any other difference between two even isotopes measured up till now. Next, the difference between ^{22}Ne and ^{20}Ne turns out to be by 40 am more negative than the most negative radius difference within the "normal" systematics. Also negative is the difference between ^{26}Mg and ^{24}Mg, before the radii differences become positive again. The sulphur isotopes $^{32-36}S$ and the argon isotopes $^{36,38}Ar$ finally are consistent again with the normal systematics. Before these results are interpreted, we turn to the systematics of isotone shifts.

B. Isotone shifts

In a similar way as isotope shifts, we have studied isotone shifts, i.e., nuclear charge radii changes when adding pairs of protons for nuclei with $20 \leq Z \leq 62$ (see Refs. [5,6]). It should be emphasized that only the method of muonic atoms is currently precise enough to reveal the subtle effects of isotone shifts. The characteristics of the systematics of isotone shifts are quite similar as for isotope shifts. Hence, a forth feature can be added to the former three mentioned in Sec. V.

(4) The behavior of isotone shifts is analogous to the behavior of isotope shifts. Both the sudden increase at the begining of a major proton shell and the nearly linear decrease within major shells are present. Due to the additional proton charges, all radii differences are shifted upwards with respect to the corresponding neutron case. While additional neutrons essentially change the polarization of the nuclear proton core, more protons obviously add on additional charge. Finally, and again analogous to the isotope shifts, the respective neutron configuration does not have a large influence on the isotone shifts.

Figure 4 shows the nuclear charge radii changes when adding pairs of protons for the region $6 \leq Z \leq 22$. Interestingly enough, the isotones in the s-d shell behave in a similar "anomalous" way as the isotopes of the same shell (see Fig. 3). There is also an excessive radius difference at $Z = 8 \rightarrow 10$ and strongly diminished differences for $Z = 10 \rightarrow 12$ and $Z = 12 \rightarrow 14$. The effect of the "anomalous" behavior has almost the same size for isotopes and isotones. In addition, the systematics at $Z = 16 \rightarrow 18$ and $Z = 18 \rightarrow 20$ behaves again "normally."

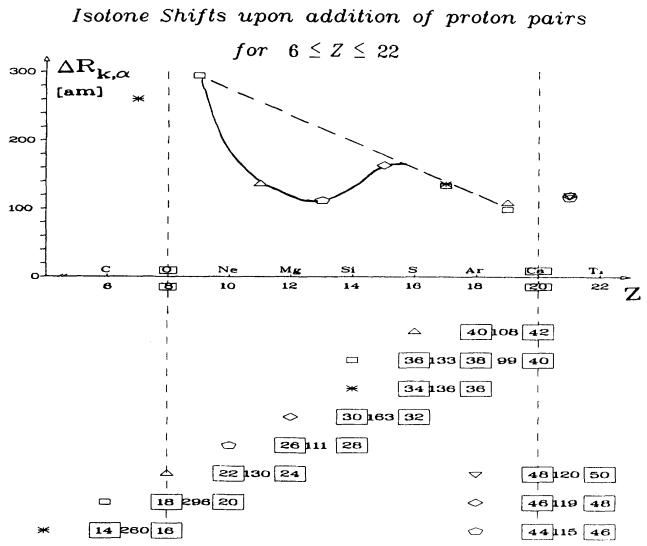

FIG. 4. "Anomalous" isotone shifts (see text) within the s-d proton shell for even-even isotones including the radii differences ^{16}O-^{14}C and Ti-Ca. Plotted are the differences of the "model-independent" (see text) equivalent Barrett radii $\Delta R_{k,\alpha}$ between two neighboring isotones with Z and $Z+2$ protons at the respective proton numbers $Z+1$. The drawn-in solid curve guides the eye. The dashed curve indicates the expected "normal" trend.

C. Odd-even staggering

In order to find out if the "anomalous" behavior of the nuclear charge radii in the s-d shell when adding pairs of nucleons is related to the first or the second nucleon added, we have to study the so-called "odd-even staggering" effect. This quantity is in muonic atom work usually defined as

$$\gamma(A+1) = \frac{[R_{k,\alpha}(A+1) - R_{k,\alpha}(A)]}{\frac{1}{2}[R_{k,\alpha}(A+2) - R_{k,\alpha}(A)]} ,$$

where A means an even mass number and $R_{k,\alpha}$ is the Barrett radius. If the radius change for the first and the second nucleon is the same, then γ is equal to 1. Usually, γ is smaller than 1, so that the contribution of the second unpaired nucleon dominates. This is the reason for the term "odd-even staggering." In the region of "normal" nuclear charge radii systematics, the γ parameters take on values between 0.2 and 0.8.

By now, it should not come as a surprise that the s-d shell nuclei show large variations in the γ parameter. As can be seen from Table V, the odd-even staggering for isotopes varies from $\gamma = -0.53$ to $\gamma = +2.48$ and for isotones from $\gamma = +0.64$ to $\gamma = +1.94$. The γ parameter for isotones cannot be negative since the addition of new charge always results in an increase of the nuclear charge size. Table V shows not only the muonic atom data, but also electron scattering data on the odd oxygen [20] and the odd chlorine [21] isotopes. If the radii changes within the s-d shell are compared when adding the first or the second unpaired nucleon, respectively, similar curves as a function of mass numbers are obtained as in Figs. 3 and 4 (for details see Ref. [23]). This fact can be interpreted as a similar contribution of the unpaired nucleons to the "anomalous" behavior within this shell. Hence, the anomaly cannot be explained by the odd-even staggering.

VI. INTERPRETATION OF THE RESULTS

In the preceding section, we have seen that the isotopes and isotones of the s-d shell behave in an "anomalous" way, that is, they do not follow the trend observed with heavier nuclei. In this section, we consider to what extent the s-d shell "anomaly" can be explained by theoretical considerations.

Semiempirical models like the "droplet model" of

TABLE V. "Odd-even staggering" parameter γ for isotopes and isotones in the s-d shell.

Z	Isotopes	γ	N	Isotones	γ
8	^{16}O-^{17}O-^{18}O	−0.21	8	^{14}C-^{15}N-^{16}O	0.76
10	^{20}O-^{21}Ne-^{22}Ne	1.46	10	^{18}O-^{19}F-^{20}Ne	1.10
12	^{24}Mg-^{25}Mg-^{26}Mg	2.48	12	^{22}Ne-^{23}Na-^{24}Mg	0.75
14	^{28}Si-^{29}Si-^{30}Si	−0.53	14	^{26}Mg-^{27}Al-^{28}Si	0.64
			16	^{30}Si-^{31}P-^{32}S	0.86
			18	^{34}S-^{35}Cl-^{36}Ar	1.94
			20	^{36}S-^{37}Cl-^{38}Ar	1.54
			20	^{38}Ar-^{39}K-^{40}Ca	0.88

Myers *et al.* [39], parametrizations as in Wesolowski [40], or correlations with binding energies by Angeli *et al.* [41], while reproducing the global trend of nuclear sizes, are generally not applicable for light nuclei. On the other hand, shell-model calculations [1–3], spherical Hartree-Fock calculations [4], and relativistic mean-field theories [42] are more promising, in particular, if deformation effects are taken into account.

For an understanding of the anomalous behavior of the nuclear charge radii in the s-d shell, a look at the subshell occupation numbers is revealing. These numbers have been calculated by Brown *et al.* [1] for both protons and neutrons for even-even nuclei. They are shown in Table VI. Obviously, there is strong mixing beyond the ^{16}O core between the three subshells, i.e., $1d_{5/2}$, $2s_{1/2}$, and $1d_{3/2}$, and there is also a strong similarity between protons and neutrons. For instance, the two additional neutrons in ^{22}Ne (compared to ^{20}Ne) and in ^{26}Mg (compared to ^{24}Mg) are preferentially added to the "inner" $1d_{5/2}$ subshell. By means of strong interaction with the protons, these two neutrons pull nuclear charge into the interior of the nucleus so that the heavier nuclei $^{22}_{10}$Ne and $^{26}_{12}$Mg become smaller in size than $^{20}_{10}$Ne and $^{24}_{12}$Mg, respectively. An analogous explanation holds for the isotone shifts between $10 \leq Z \leq 14$, specifically for the isotone pairs $^{24}_{12}$Mg-$^{22}_{10}$Ne and $^{28}_{14}$Si-$^{26}_{12}$Mg, accounting for the dip in the isotone curve of Fig. 4. Toward the end of the s-d shell, i.e., for $Z,N > 14$, the $1d_{5/2}$ subshell becomes practically saturated. The successive population of the higher-lying $2s_{1/2}$ and $1d_{3/2}$ subshells then leads to "normal" charge radii increases, as expected from the systematics of heavier nuclei.

TABLE VI. Shell occupation numbers of protons and neutrons beyond the ^{16}O core for the even-even nuclei of the s-d shell as calculated by Brown *et al.* [1]. The lengths of the drawn-in bars are proportional to the respective occupation numbers.

nucleus	protons			neutrons		
	$1d_{5/2}$	$2s_{1/2}$	$1d_{3/2}$	$1d_{5/2}$	$2s_{1/2}$	$1d_{3/2}$
$^{20}_{10}$Ne$_{10}$	1.21	0.51	0.28	1.21	0.51	0.28
$^{22}_{10}$Ne$_{12}$	1.40	0.42	0.18	3.18	0.39	0.43
$^{24}_{12}$Mg$_{12}$	2.99	0.45	0.56	2.99	0.45	0.56
$^{26}_{12}$Mg$_{14}$	3.20	0.35	0.45	4.82	0.56	0.62
$^{28}_{14}$Si$_{14}$	4.62	0.70	0.68	4.62	0.70	0.68
$^{30}_{14}$Si$_{16}$	4.74	0.68	0.58	5.15	1.41	1.44
$^{32}_{16}$S$_{16}$	5.42	1.42	1.16	5.42	1.42	1.16
$^{34}_{16}$S$_{18}$	5.61	1.66	0.73	5.76	1.76	2.48
$^{36}_{18}$Ar$_{18}$	5.54	1.78	2.68	5.54	1.78	2.68

Besides strong subshell mixing, the nuclei in the s-d shell are also characterized by strong intrinsic deformations. These deformations change from an oblate, disklike shape to a prolate shape as manifested by the sign of their ground-state quadrupole moments. Diminishing deformations towards the end of a given shell have already been evoked as a reason for smaller nuclear charge radii when adding pairs of neutrons [5,24].

In order to compare the results of the spherical shell-model calculations of Carchidi *et al.* [3] or the Hartree-Fock (HF) calculations of Friedrich [4] with our experimentally measured charge radii, the contributions due to intrinsic nuclear deformations have to be taken explicitly into account. For this purpose, we correct the calculated spherical rms radii by a deformed part. Specifically, we employ the "pairing-plus-quadrupole model" of Reehal and Sorensen [43], where the nuclei are described by homogeneously charged rotational ellipsoids, with the deformation limited to the quadrupole contribution. The rms radii can then be written as

$$\langle r^2 \rangle_{s+d} = \langle r^2 \rangle_s \left[1 + \frac{5}{4\pi} \langle \beta_2^2 \rangle \right] ,$$

where the indices s and d stand for "spherical" and "deformed," respectively. The quadrupole deformation parameter $\langle \beta_2^2 \rangle$ is given by [43]

$$\langle \beta_2^2 \rangle = \left[\frac{4\pi}{5} \right]^2 \frac{1}{Z^2} (\langle r^2 \rangle_s)^{-2} B(E2, 0^+ \rightarrow 2^+) .$$

If the $B(E2)$ matrix elements are evaluated from the lifetimes and the branching ratios of the respective excited nuclear states [44,45], and if the spherical rms radii $\langle r^2 \rangle_s$ are taken from theory, e.g., from the HF calculations of Friedrich [4,46], Table VII is obtained. In this table, volume and deformation contributions to the rms radii calculated in the manner described above are presented for all stable even-even nuclei of the s-d shell. Also shown are the deformation factors

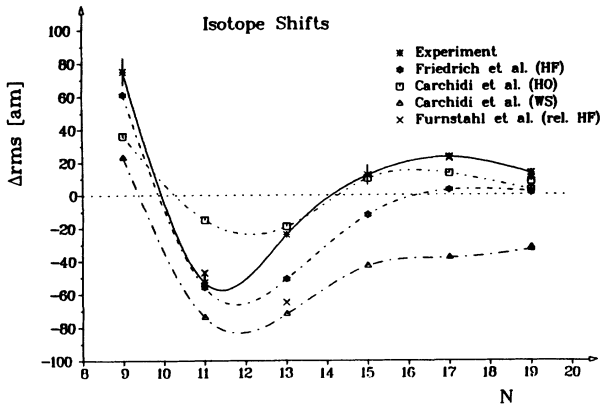

FIG. 5. Comparison of our measured isotopes shift $\Delta\langle r^2\rangle^{1/2}$ (the curve guides the eye) within the s-d neutron shell with deformation-corrected HF calculations of Friedrich *et al.* [4,46] deformation-corrected harmonic-oscillator-(HO-) and Woods-Saxon- (WS-) type shell-model calculations of Carchidi *et al.* [3], and relativistic mean-field calculations of Furnstahl *et al.* [42] (rel. HF).

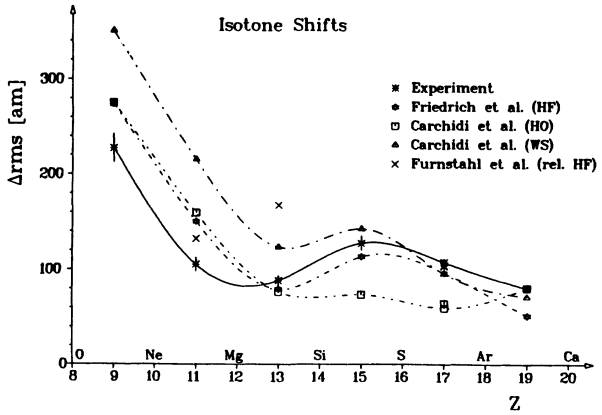

FIG. 6. Comparison of our measured isotone shifts $\Delta\langle r^2\rangle^{1/2}$ (the curve guides the eye) within the s-d proton shell with deformation-corrected HF calculations of Friedrich *et al.*, deformation-corrected harmonic-oscillator- (HO-) and Woods-Saxon- (WS-) type shell-model calculations of Carchidi *et al.*, and relativistic mean-field calculations of Furnstahl *et al.* (rel. HF).

$$\left[1+\frac{5}{4\pi}\langle\beta_2^2\rangle\right]^{1/2}$$

and the resulting increase of the rms radii. It is interesting to note that the changes due to deformation can be at least as important as the changes in the spherical parts between neighboring nuclei. The next two figures (5 and 6) compare these deformation-corrected HF calculations of Friedrich with our muonic atom radii changes for the even isotopes and isotones of the s-d shell. There is gen-

TABLE VII. Volume and deformation contributions to the total rms radii. The spherical radii are taken from the Hartree-Fock calculations of Friedrich [4,46]; the deformed parts are calculated according to the pairing-plus-quadrupole model [43] with the deformation factor $[1+(5/4\pi)\langle\beta_2^2\rangle]^{1/2}$.

Nucleus	Spherical rms radius (fm)	Deformation factor	Δrms by deformation (fm)	rms radius $\langle r^2\rangle^{1/2}_{s+d}$ (fm)	Δrms (fm)
$^{16}_{8}$O				2.742	
					+0.061
$^{18}_{8}$O	2.734	1.0253	0.069	2.803	
					+0.274
$^{20}_{10}$Ne	2.928	1.0509	0.149	3.077	
					−0.056
$^{22}_{10}$Ne	2.905	1.0398	0.116	3.021	
					+0.149
$^{24}_{12}$Mg	3.029	1.0466	0.141	3.170	
					−0.051
$^{26}_{12}$Mg	3.018	1.0334	0.101	3.119	
					+0.079
$^{28}_{14}$Si	3.125	1.0233	0.073	3.198	
					−0.013
$^{30}_{14}$Si	3.134	1.0164	0.051	3.185	
					+0.114
$^{32}_{16}$S	3.249	1.0153	0.050	3.299	
					+0.002
$^{34}_{16}$S	3.268	1.0102	0.033	3.301	
					+0.002
$^{36}_{16}$S	3.290	1.0041	0.013	3.303	
					+0.095
$^{36}_{18}$Ar	3.366	1.0094	0.032	3.398	
					+0.001
$^{38}_{18}$Ar	3.381	1.0053	0.018	3.399	

erally good agreement between experiment and theory. In both cases, the dip around $N,Z \cong 12$, including the negative values in the isotope shifts, is reproduced. Also presented in these figures are harmonic-oscillator and Woods-Saxon shell-model calculations by Carchidi *et al.* [3], corrected for deformation. They both show also the *s-d* shell anomaly, but agree somewhat less with our data. Finally, the relativistic mean-field calculations of Furnstahl *et al.* [42], which already contain deformation, also yield negative rms changes for the isotope shifts, but are not in accordance for the isotone shifts.

Regarding odd-even staggering, i.e., the different influences of the first and the second unpaired nucleon on the charge radii, we have compared the shell-model calculations of Carchidi *et al.* [3] with our muonic atom data. Again, there is a reasonable agreement with theory, if the intrinsic deformations are explicitly taken into account. In particular, the harmonic-oscillator-type calculations yield closer agreement with experiment than the Woods-Saxon-type calculations. Figures are not given in this paper; for more details see Ref. [23].

Hence, we can conclude that our nuclear charge radii differences measured by means of the muonic atom x-ray method within the *s-d* shell are reasonably well described by theoretical Hartree-Fock and shell-model calculations, if both configuration mixing between the three subshells ($1d_{5/2}$, $2s_{1/2}$, and $1d_{3/2}$) as well as deformation changes are taken into account. The "anomaly" within the *s-d* shell with respect to the "normal" systematics of the nuclear charge radii of heavier nuclei can thus be understood.

ACKNOWLEDGMENTS

The authors acknowledge fruitful discussions with Professor H. Schneuwly, Fribourg, and Dr. E. B. Shera, Los Alamos National Laboratory. They appreciate the loan of the ^{26}Mg target by Dr. U. Berg of the University of Giessen and the isotopic analyses of the employed Mg targets by Professor F. Begemann and K. Kallas, Max Planck Institut, Mainz. They particularly thank Professor J. Friedrich, Institut für Kernphysik, Universität Mainz, for his spherical Hartree-Fock calculations using the Skyrme G_σ force. The experiment has been supported by the Bundesministerium für Forschung und Technologie and the Swiss National Foundation.

[1] B. A. Brown, R. Radhi, and B. H. Wildenthal, Phys. Rep. **101**, 313 (1983).
[2] B. A. Brown, C. R. Bronk, and P. E. Hodgson, J. Phys. G **10**, 1683 (1984).
[3] M. Carchidi, B. H. Wildenthal, and B. A. Brown, Phys. Rev. C **34**, 2280 (1986).
[4] J. Friedrich and P. G. Reinhard, Phys. Rev. C **33**, 335 (1986).
[5] H. J. Emrich, G. Fricke, M. Hoehn, K. Kaeser, M. Mallot, H. Miska, B. Robert-Tissot, D. Rychel, L. A. Schaller, L. Schellenberg, H. Schneuwly, E. B. Sheara, H. G. Sieberling, R. Steffen, H. D. Wohlfahrt, and Y. Yamazaki, in *Proceedings of the 4th International Conference on Nuclei far from Stability*, Helsingor, 1981, edited by L. O. Skolen, p. 33.
[6] G. Fricke, C. Bernhardt, T. Hack, T. Hennemann, J. Herberz, J. Jansen, R. Klein, P. Mazanek, L. Schellenberg, R. Jacot-Guillarmod, C. Piller, L. A. Schaller, and H. Schneuwly, Verh. DPG (VI) **25**, 1443 (1990).
[7] C. Piller, R. Jacot-Guillarmod, L. A. Schaller, L. Schellenberg, H. Schneuwly, G. Fricke, T. Hennemann, J. Herberz, R. Klein, M. Reutter, and E. B. Shera, Verh. DPG (VI) **25**, 1442 (1990).
[8] C. Piller, C. Gugler, R. Jacot-Guillarmod, L. A. Schaller, L. Schellenberg, H. Schneuwly, G. Fricke, T. Hennemann, and J. Herberz, Phys. Rev. C **42**, 182 (1990).
[9] L. Schellenberg, B. Robert-Tissot, K. Kaeser, L. A. Schaller, H. Schneuwly, G. Fricke, S. Glückert, G. Mallot, and E. B. Sheara, Nucl. Phys. **A333**, 333 (1980).
[10] E. B. Shera, E. T. Ritter, R. B. Perkins, G. A. Rinker, L. K. Wagner, H. D. Wohlfahrt, G. Fricke, and R. M. Steffen, Phys. Rev. C **4**, 731 (1976).
[11] E. B. Shera, M. V. Hoehn, G. Fricke, and G. Mallot, Phys. Rev. C **39**, 195 (1989).
[12] H. D. Wohlfahrt, E. B. Shera, M. V. Hoehn, Y. Yamazaki, and R. M. Steffen, Phys. Rev. C **23**, 533 (1981).
[13] L. A. Schaller, L. Schellenberg, A. Rüetschi, and H. Schneuwly, Nucl. Phys. **A343**, 333 (1980).
[14] L. A. Schaller, L. Schellenberg, T. Q. Phan, G. Piller, A. Rüetschi, and H. Schneuwly, Nucl. Phys. **A379**, 523 (1982).
[15] L. A. Schaller, D. A. Barandao, P. Bergem, M. Boschung, T. Q. Phan, G. Piller, A. Rüetschi, L. Schellenberg, H. Schneuwly, G. Fricke, G. Mallot, and H. G. Sieberling, Phys. Rev. C **31**, 1007 (1985).
[16] G. Fricke, G. Mallot, T. Q. Phan, L. Schellenberg, G. Piller, A. Rüetschi, L. A. Schaller, and H. Schneuwly, Verh. DPG (VI) **17**, 1145 (1982).
[17] G. Backenstoss, W. Kowald, I. Schwanner, L. Tauscher, H. J. Weyer, D. Gotta, and R. Guigas, Phys. Lett. **95B**, 212 (1980).
[18] R. D. Ehrlich, Phys. Rev. **173**, 1088 (1968).
[19] H. de Vries, C. W. de Jager, and C. de Vries, At. Data Nucl. Data Tables **36**, 495 (1987).
[20] H. Miska, B. Norum, M. V. Hynes, W. Bertozzi, S. Kowalsky, F. N. Rad, C. P. Sargent, T. Sasanuma, and B. L. Berman, Phys. Lett. **83B**, 165 (1979).
[21] W. J. Briscoe, H. Crannel, and J. C. Bergstrom, Nucl. Phys. **A344**, 475 (1980).
[22] J. Herberz, Diplomarkeit, Universität Mainz, KPH 10/86, 1986.
[23] J. Herberz, Promotionsarbeit, Universität Mainz, KPH 6/89, 1989.
[24] G. Mallot, Diplomarkeit, Universität Mainz, KPH 21/80, 1980.
[25] H. Kumahora, Nucl. Instrum. Methods **A238**, 431 (1985).
[26] R. G. Helmer, P.H.M. van Assche, and C. van der Leun, At. Data Nucl. Data Tables **24**, 39 (1979).
[27] W. Reichart, computer code DAVID, Zürich/PSI, 1984 (unpublished).
[28] G. Mallot and T. Hennemann, computer codes CONFIT, DISPLAY, and MYFIT, Mainz, 1989 (unpublished).

[29] T. Hennemann and G. Mallot, modified computer code MZMUON2 of Y. Tanaka, The formalism of MUON2 and XRAY2, Los Alamos, 1984 (unpublished).
[30] P. Bergem, G. Piller, A. Rüetschi, L. A. Schaller, L. Schellenberg, and H. Schneuwly, Phys. Rev. C **37**, 2821 (1988).
[31] E. F. Borie and G. A. Rinker, Rev. Mod. Phys. **54**, 67 (1982).
[32] R. C. Barrett, Phys. Lett. **33B**, 388 (1970).
[33] E. A. Knight, R. P. Singhal, R. G. Arthur, and M.W.S. Macauley, J. Phys. G **7**, 1115 (1981).
[34] R. Soundranayagam, A. Saha, Kamal K. Seth, C. W. de Jager, H. de Vries, H. Blok, and G. van der Steenhoven, Phys. Lett. B **212**, 13 (1988).
[35] I. Angeli, Z. Phys. **A334**, 377 (1989).
[36] J. L. Friar and J. W. Negele, Nucl. Phys. **A240**, 301 (1975).
[37] E.A.J.M. Offermann, L. S. Cardman, C. W. de Jager, H. Miska, C. de Vries, and H. de Vries, Phys. Rev. C **44**, 1096 (1991).
[38] W. Ruckstuhl, B. Aas, W. Beer, I. Beltrami, F.W.N. de Boer, K. Bos, P.F.A. Goudsmit, U. Kiebele, H. J. Leisi, G. Strassner, A. Vacchi, and R. Weber, Phys. Rev. Lett. **49**, 859 (1982).
[39] W. D. Myers and K. H. Schmidt, Nucl. Phys. **A410**, 61 (1983).
[40] E. Wesolowski, J. Phys. G **11**, 909 (1985).
[41] I. Angeli and R. J. Lombard, Z. Phys. A **324**, 299 (1986).
[42] R. J. Furnstahl, C. E. Price, and G. E. Walker, Phys. Rev. C **36**, 2590 (1987).
[43] B. S. Reehal and R. A. Sorensen, Nucl. Phys. **A161**, 385 (1971).
[44] P. M. Endt and C. van der Leun, Nucl. Phys. **A310**, 1 (1978).
[45] P. M. Endt, At. Data Nucl. Data Tables **23**, 3 (1979).
[46] J. Friedrich, private communications, Mainz, 1989.